

Interferometric observations of the Mira star α Ceti with the VLTI/VINCI instrument in the near-infrared

H.C. Woodruff^a, M. Eberhardt^a, T. Driebe^a, K.-H. Hofmann^a, K. Ohnaka^a, A. Richichi^b,
D. Schertl^a, M. Schöller^c, M. Scholz^{d,e}, G. Weigelt^a, M. Wittkowski^b, P. R. Wood^f,

^aMax-Planck-Institut für Radioastronomie, Auf dem Hügel 69, D-53321 Bonn, Germany;

^bEuropean Southern Observatory, Karl-Schwarzschildt-Str. 2, D-85748 Garching, Germany;

^cEuropean Southern Observatory, Casilla 19001, Santiago 19, Chile;

^dInstitut für Theoretische Astrophysik, Universität Heidelberg, Tiergartenstr. 15, D-69121 Heidelberg, Germany;

^eInstitute of Astronomy, School of Physics, University of Sydney NSW 2006, Australia;

^fResearch School of Astronomy and Astrophysics, Australian National University, Cotter Road, Weston Creek ACT 2611, Australia

ABSTRACT

We present K -band commissioning observations of the Mira star prototype α Ceti obtained at the ESO Very Large Telescope Interferometer (VLTI) with the VINCI instrument and two siderostats. The observations were carried out between 2001 October and December, in 2002 January and December, and in 2003 January. Rosseland angular radii are derived from the measured visibilities by fitting theoretical visibility functions obtained from center-to-limb intensity variations (CLVs) of Mira star models of Bessel et al.¹(=BSW), Hofmann et al.²(=HSW), and Tej et al.³(=TLSW). Using the derived Rosseland angular radii and the SEDs reconstructed from available photometric and spectrophotometric data, we find effective temperatures ranging from $T_{\text{eff}} = 3192 \pm 200$ K at phase $\Phi = 0.13$ to 2918 ± 183 K at $\Phi = 0.26$. Comparison of these Rosseland radii, effective temperatures, and the shape of the observed visibility functions with model predictions suggests that α Ceti is a fundamental mode pulsator. Furthermore, we investigated the variation of visibility function and diameter with phase. The Rosseland angular diameter of α Ceti increased from 28.9 ± 0.3 mas (corresponding to a Rosseland radius of $332 \pm 38 R_{\odot}$ for a distance of $D = 107 \pm 12$ pc) at $\Phi = 0.13$ to 34.9 ± 0.4 mas ($402 \pm 46 R_{\odot}$) at $\Phi = 0.4$. The error of the Rosseland linear radius almost entirely results from the error of the parallax, since the error of the angular diameter is only approximately 1%.

Keywords: interferometry, Mira stars, near-infrared, VLTI/VINCI

1. INTRODUCTION

Mira stars are long-period variables (LPVs) which evolve along the asymptotic giant branch (AGB), and are characterized by stellar pulsation with amplitudes as large as $\Delta V \sim 9$ and well-defined pulsation periods (80–1000 days). In recent years, the comparison of theoretical pulsation models with MACHO observations of LPVs in the LMC, in particular the reproduction of period ratios in multimode pulsators, has shown that Miras are fundamental-mode pulsators.⁴ However, radius measurements of Mira variables when compared to theoretical pulsation calculations have generally yielded the large values expected for first overtone pulsators.^{5,6} Thus, there is clearly a problem with the interpretation of radius measurements that needs examination.

High-resolution interferometric studies of Mira stars allow the determination of the size of the stellar disk, its center-to-limb intensity variation, surface inhomogeneities, and the dependence of diameter on wavelength and variability phase^{7–9} (for a more extended list of references see Ref. 23). The results of such interferometric observations can be compared with predictions from theoretical models of stellar pulsation and the atmosphere of Mira stars.^{1–3, 10–13} Confrontation of detailed theoretical models with high-resolution observations is crucial

Further author information: (Send correspondence to Thomas Driebe)

Thomas Driebe: E-mail: driebe@mpifr-bonn.mpg.de, Telephone: +49-228-525-353

for improving our understanding of the physical properties of Mira stars.^{14–17}

Here, we present ESO VLTI/VINCI visibility measurements of *o* Cet and compare the measured visibility shape and the phase dependence of the visibility with model predictions. *o* Cet, the prototype of oxygen-rich Mira stars, is a very suitable object for these studies, since VINCI observations exist for different phases and baselines, its distance is known (revised HIPPARCOS distance 107.06 ± 12.26 pc¹⁸), and a large amount of spectroscopic and photometric data is available for different phases.

2. OBSERVATIONS AND DATA REDUCTION

A total of 48 visibility measurements of *o* Cet were carried out with VINCI¹⁹ at the VLTI in the commissioning period between 2001 October and 2003 January. All this data has been publicly released. Projected baselines ranging from 7.5 to 16.0 m were employed. VINCI is a fiber-optics beam combiner instrument based on the concept of the FLUOR instrument.^{20,21} With the single-mode fibers to spatially filter the wavefronts perturbed by atmospheric turbulence, this beam combiner provides accurate visibility measurements in spite of time-variable atmosphere conditions. As an example, the visibilities of *o* Cet vs. spatial frequency measured at two different phases are displayed in Fig. 1.

In addition to the VINCI observations, we recorded speckle interferograms of *o* Cet on 2003 October 7 with the SAO 6 m telescope in Russia. The speckle camera used for the observations was equipped with a Rockwell HAWAII array. The field of view of the recorded speckle interferograms was $11''.02$. A filter with a central wavelength of 2086 nm and a width of 20 nm was used. The exposure time per frame was 10 ms. The complete data set consists of 100 speckle interferograms of *o* Cet and 360 of an unresolved reference star (HD 14652). The seeing (FWHM) was $\sim 3''.4$. The visibilities (see Fig. 1b) were obtained using the speckle interferometry method.²²

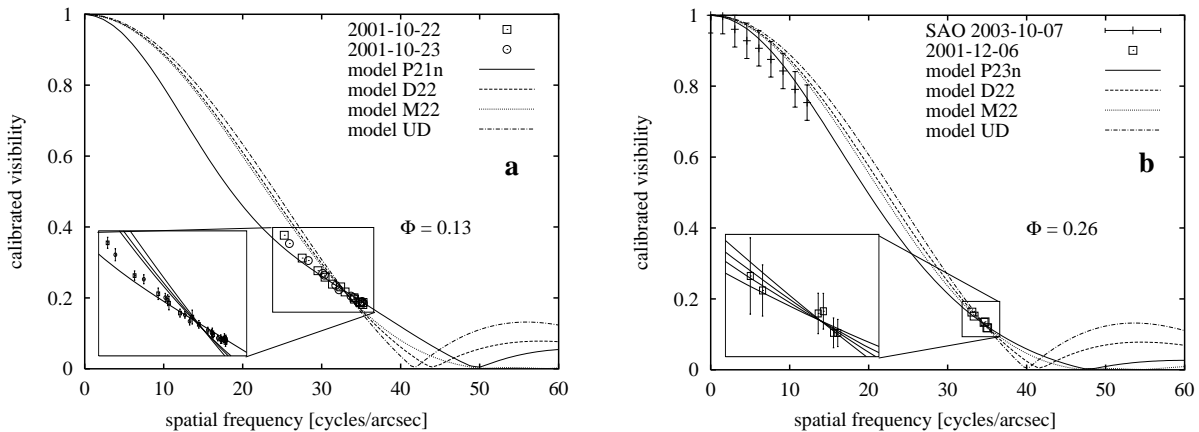


Figure 1. Visibilities of *o* Cet vs. spatial frequency measured with VLTI/VINCI at phase 0.13 (a, observation dates 2001 Oct 22/23), and at phase 0.26 (b, observation date 2001 Dec 06) together with SAO speckle interferometry data²³ measured at the same phase but at a different cycle (observation date 2003 Oct 07; data not used for the model visibility fit). The insets show an enlargement of the relevant spatial frequency range. Here, the error bars are included. Solid lines represent the P models from Ref. 3 and 14 (=ISW hereafter), dashed lines the D models from BSW,¹ dotted lines the M models from HSW, and the dash-dotted lines represent the simple uniform-disk model CLVs (see discussion in Sect. 3). Note that from our SAO observations there is no indication for a visibility contribution from a circumstellar dust shell at low spatial frequencies.

Processing of the raw VINCI data for estimating the coherence factors μ (i.e. the fringe contrast or uncalibrated visibility) was carried out with the VINCI data reduction software provided by the European Southern Observatory* (version 2.0.6), based on wavelets transforms to derive the power spectral density. The processing of a series of OPD scans yields the uncalibrated squared visibility μ^2 for each individual scan, and the averaged value $\langle \mu^2 \rangle$ is used to derive the calibrated visibility.^{24,25}

* www.eso.org/~pballest/vinci

The squared transfer functions T^2 , which account for instrumental and atmospheric effects, were derived from measurements of calibrator stars and their known angular diameters. The expected calibrator visibility V_{cal} was calculated from uniform disk (UD) angular diameters of the calibrators,²⁶ and the transfer function was evaluated as $T^2 = \mu_{\text{cal}}^2 / V_{\text{cal}}^2$, where μ_{cal} is the measured uncalibrated visibility of the calibrator. Details on the calibrators of the nights on which *o* Cet was measured and their diameters are given in Ref. 23. The errors of the individual transfer function values were calculated from the errors of the raw visibilities and the errors of the uniform-disk visibilities of the calibrators which arise from the uncertainties of the corresponding uniform-disk diameters. For most of the individual transfer function values, the error contributions of the raw visibility and the uniform-disk visibility of the calibrator are of the same order, resulting in total errors of typically $\lesssim 5\%$. Only in a few cases the error contribution of either the raw visibility or the uniform-disk visibility of the calibrator is significantly larger, resulting in much larger errors of the transfer function values.

The final errors (see Fig. 1) of the calibrated visibilities were derived from simple Gaussian error propagation of the error of the fits to the measured transfer function values and the error of the uncalibrated visibility.

3. COMPARISON OF THE OBSERVATIONS WITH MIRA STAR MODELS

3.1. Mira star models

All Mira star models used in this paper are from BSW¹ (D and E series), HSW² (P, M, and O series), TLSW³ (P series), and from ISW¹³ (P series). They were developed as possible representations of *o* Cet and hence have periods P close to 332 days. These models differ in pulsation mode, stellar mass M , parent star radius R_p (i.e., radius of the initial non-pulsating model), and luminosity L . The parent-star luminosities of the model series had been chosen based on considerations of the period-luminosity-relation for the LMC and a theoretical metallicity correction (BSW,¹ HSW²). Solar abundances were assumed for all models. The five model series represent stars pulsating in the fundamental mode (f ; D, P, and M) or in the first overtone mode (o ; E and O). All models are named after the cycle and phase they represent. For example, P28 denotes the P model calculated near visual phase 0.8 in the second cycle. The suffix “n”, (e.g., P11n), denotes the new models from the recent fine phase grid of ISW.¹³ Further details on the model properties are given in Ref. 23.

The Rosseland angular radii R_{Ross}^a of *o* Cet were determined in the following way: first, we derived the K -band angular radius R_K^a , which is defined as the FWHM of the model CLV. The R_K^a values (corresponding to different model-phase combinations) were determined by least-square fits between the measured Mira visibilities and the visibilities of the corresponding model CLVs. Then, the Rosseland angular radii R_{Ross}^a were derived from the obtained K -band angular radii and from the theoretical ratios R_{Ross}/R_K provided by the models. For a more detailed description of the visibility fitting procedure we refer to HSW.²

3.2. Comparison of observed and model Rosseland linear radii

Linear Rosseland radii of *o* Cet were obtained using the derived angular radii together with Mira’s revised HIPPARCOS parallax of 9.34 ± 1.07 mas.^{18,27} The comparison between the derived Rosseland linear radii and those of the corresponding models which provided the CLVs reveals good agreement for the fundamental-mode M series for the phases $\Phi = 0.13 - 0.26$ and 1.47 , whereas the predicted radii are systematically too small at the phases 0.4 and 1.4 . The P-series models from HSW,² TLSW,³ and ISW¹³ predict, in most cases (i.e., 10 out of 14 cycle-phase combinations), Rosseland linear radii which agree with the measured values within the error bars. This good agreement of the P models is independent of the phase grid spacing. The Rosseland linear radii predicted from the M models agree with the measured values (within the error bars) in 8 out of 12 cycle-phase combinations. Thus, our radius comparison favors the fundamental-mode pulsation P and M models as possible representations of Mira, whereas all first overtone pulsation model series can be ruled out as models that reliably predict the Rosseland radius of *o* Cet.

3.3. Determination of T_{eff}

The effective temperature T_{eff} of a star can be derived from its Rosseland angular diameter and its bolometric flux.^{17,28,29} In order to estimate the bolometric flux, we used photometric measurements of *o* Cet in the visual³⁰ and, when available, in the NIR in combination with the ISO spectrum ranging from $2.36 \mu\text{m}$ to $45.38 \mu\text{m}$. Since the ISO spectrum was taken at maximum light ($\Phi = 0$), we used light curves³¹ obtained with the Diffuse Infrared

Background Experiment (DIRBE³²) to estimate the variability of *o* Cet in the ISO spectral range. Also included in our SED analysis are spectrophotometric data in the wavelength region between 0.44 μm and 1.08 μm ,^{33–36} and *JHK* photometry data between 1.25 and 2.2 μm .³⁷ Since most of the bolometric flux comes from the NIR, the error of F_{bol} induced by flux density changes in the ISO range makes a contribution of only $\sim 5 - 10\%$ to the total error. Because of the small interstellar extinction in the *V* and *K* bands and the proximity of Mira, no correction for interstellar extinction was applied. Integration of the SED yields $F_{\text{bol}} = 2.63 \cdot 10^{-8} \text{ Wm}^{-2}$ at $\Phi = 0.13$, $F_{\text{bol}} = 2.41 \cdot 10^{-8} \text{ Wm}^{-2}$ at $\Phi = 0.18$, and $F_{\text{bol}} = 2.36 \cdot 10^{-8} \text{ Wm}^{-2}$ at $\Phi = 0.26$. The total error of the bolometric flux was estimated to be 25%. The error sources are mainly the cycle and phase uncertainties of the spectrophotometric and photometric observations. The error in T_{eff} is 6% when errors of approximately 25% and 1% are assumed for F_{bol} and $d_{\text{Ross}}^{\text{a}}$, respectively.

Our temperature analysis reveals that the T_{eff} values of the D model series are very close (within the error bars) to those derived from the observations at all phases. Although the P11n model shows agreement between observation and theory for phase 0.13, all other cycle-phase combination of the P-model series as well as all other model series yield large differences between theoretical and measured effective temperature values.

We also determined the luminosity range of *o* Cet for the observed phases from its bolometric flux and HIPPARCOS parallax ($9.34 \pm 1.07 \text{ mas}^{18}$). We obtained $9360 \pm 3140 L_{\odot}$ for $\Phi = 0.13$ and $8400 \pm 2820 L_{\odot}$ for $\Phi = 0.26$. These luminosities are higher than those predicted by all models for the respective phases except for the E model series, for which a higher luminosity of the parent star was adopted.

3.4. CLVs and visibility shapes

As discussed in Sect. 3.2, there is good agreement between the derived Rosseland linear radii and the Rosseland linear radii predicted by model series P and M series models, while there is little or no agreement for the other models. On the other hand, the effective temperatures derived from observations are close to those predicted by the D-model series. In this section we investigate whether one of the model series can be favored by comparing the observed and theoretical visibility shapes.

The measured visibilities at two different phases within the first cycle of observations are shown in Fig. 1, together with fitted model visibility curves for the P, M, and D models. The P-series fundamental pulsator mode model P21n shows much better agreement with the observation at $\Phi = 0.13$ than the D and M models or simple UD model CLVs. This can be clearly seen from the inset in Fig. 1, and a comparison of the reduced χ^2 values for the different model fits. For phase $\Phi = 0.26$ (Fig.1b) and all other phases analyzed the small number of visibility points and the insufficient coverage of the spatial frequency domain make it impossible to draw conclusions about which model series should be favored. It should be noted that the agreement of the observed CLV shape with the P-series model CLV shape is also better than for the E and O first-overtone model series, which were already ruled out from radius and temperature comparisons.

The visibility can also be affected by a circumstellar dust shell which is not included in the model calculations. A dust shell could cause a narrow visibility peak at low spatial frequencies. Therefore, we measured the visibilities of *o* Cet using our speckle camera at the SAO 6 m telescope. These additional visibilities cover the low spatial frequency domain, showing that the use of dust-free CLV models is justified (see Fig. 1b).

Although the measured visibility shape for $\Phi = 0.13$ is in good agreement with the predictions made by the P21n model, we nevertheless wish to point out that the observed visibility shape can also be affected by deviations from circular symmetry of the intensity distribution. Therefore, we studied possible effects of such asymmetries on the visibility shapes by assuming elliptical uniform-disk intensity distributions with ratios of minor to major axis between 0.7 and 1.0. It turned out that the observed visibilities cannot be reproduced by such elliptical uniform disk intensity distributions. However, we note that this study cannot exclude the presence of other types of asymmetries in Mira, such as surface inhomogeneities produced by giant convective cells.³⁸

3.5. Diameter-phase relationship

Taking the Rosseland diameters derived with the P model CLVs at the four different phases within the first cycle, we obtained the diameter-phase relationship presented in Fig. 2. The figure clearly shows a monotonic increase of the Rosseland angular diameter with decreasing brightness from phase $\Phi = 0.13$ ($d_{\text{Ross}}^{\text{a}} = 28.9 \pm 0.3 \text{ mas}$, corresponding to a Rosseland linear radius of $R_{\text{Ross}} = 332 \pm 38 R_{\odot}$) to phase $\Phi = 0.40$ ($d_{\text{Ross}}^{\text{a}} = 34.9 \pm 0.4 \text{ mas}$, $R_{\text{Ross}} = 402 \pm 46 R_{\odot}$). Therefore, as the visual intensity decreases, the *K*-band diameter of *o* Cet increases.

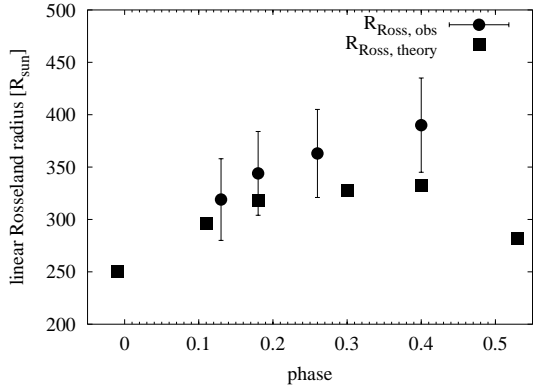


Figure 2. Linear Rosseland radii of *o* Cet derived from P21n, P22, P23n, and P24n series models (filled circles) at four different phases ($\Phi = 0.13$: $R_{\text{Ross}} = 332 \pm 38 R_{\odot}$; $\Phi = 0.18$: $R_{\text{Ross}} = 354 \pm 41 R_{\odot}$; $\Phi = 0.26$: $R_{\text{Ross}} = 370 \pm 42 R_{\odot}$; $\Phi = 0.40$: $R_{\text{Ross}} = 402 \pm 46 R_{\odot}$) and theoretical P2x models (filled squares). The diagram clearly shows a monotonic increase of radius with decreasing brightness, in line with the predictions from TLSW.³

From our analysis we find an 18% increase of the diameters of *o* Cet between $\Phi = 0.13$ and $\Phi = 0.40$, which is quite similar to the recently detected diameter increase for the oxygen-rich Mira star S Lac³⁹ of approximately 14% for the corresponding phase range.

The intensity profiles of the best fitting models for the two phases $\Phi = 0.13$ and 0.26 , which were found to be the P21n and P23n series models, are shown in Fig. 3. The P models are among those with the lowest effective temperatures and exhibit extended faint wings near maximum light ($\Phi = 0.0$) and protrusions near minimum light ($\Phi = 0.5$). The extended wing in the intensity profile at maximum light is mainly caused by water molecules, which are one of the most abundant molecules in the atmospheres of oxygen-rich Miras.⁴⁰ From the analysis of the ISO spectrum, it can be concluded⁴¹ that H_2O layers are more extended at maximum light. This is in agreement with the CLV near maximum light (Fig. 3a). As the visual brightness decreases from maximum to minimum phase, the effective temperature decreases, and the extended wings are less pronounced. From $\Phi = 0.18$ to $\Phi = 0.40$, water absorption increases strongly behind the shock front. This results (i) in a protrusion of the CLV shape (“Gaussian-type” CLV) and (ii) in substantial molecular-band blanketing of continuum windows and an increase of R_{Ross}^a , whose position is marked by arrows in Fig. 3. The CLVs predicted by the M models have comparable protrusions, and although the M model visibility fits to the observed visibilities do not show good agreement, they yield Rosseland linear radii which agree with the theoretical Rosseland linear radii. Because of higher temperatures and lower densities, the D models do not exhibit the protrusions seen in the P and M models. Therefore, the slope of the visibility is not as flat as in the case of P and M models. For a more detailed description of the different model CLVs, we refer to, e.g., BSW¹ and TLSW.³

4. CONCLUSIONS

We presented *K*-band observations of *o* Cet obtained with the VLTI and its beam combiner instrument VINCI. From these VINCI observations at six different epochs we derived Rosseland angular radii using 5 different theoretical model series.^{1–3,13} Using the derived Rosseland angular diameter and the SEDs reconstructed from various photometry and spectrophotometry data, we obtained effective temperatures ranging from $T_{\text{eff}} = 3192 \pm 200$ K at $\Phi = 0.13$ to 2918 ± 183 K for $\Phi = 0.26$.

We found that there is fair agreement between the Rosseland linear radii derived from the observed visibilities and those predicted by the fundamental mode pulsation model series P and M, while there is no agreement for other models. The nonlinear pulsation models all start from a static “parent” star. The parent star for the best-fitting model series, the fundamental-mode P series, has a radius of $\sim 240 R_{\odot}$. It is clear from Fig. 4 that *o* Cet, and indeed the nonlinear pulsation models from the P series, nearly all have radii of ~ 300 – $400 R_{\odot}$. Thus, the effect of large amplitude pulsation is to expand the surface layers of the star so that its apparent radius is considerably larger at most phases than the radius it would have if static. This expansion of the apparent radius does not greatly affect the interior of the model or the pulsation period. Hence, if one compares observed radii of Miras in (say) a radius-period diagram with the radii and pulsation periods of the parent stars, then one will clearly not find agreement. This is the reason that the Miras were thought for so long to be first-overtone pulsators.^{42,43} It is only by a detailed comparison of interferometric angular diameter measurements with models of large-amplitude, pulsating atmospheres that this problem has been solved.

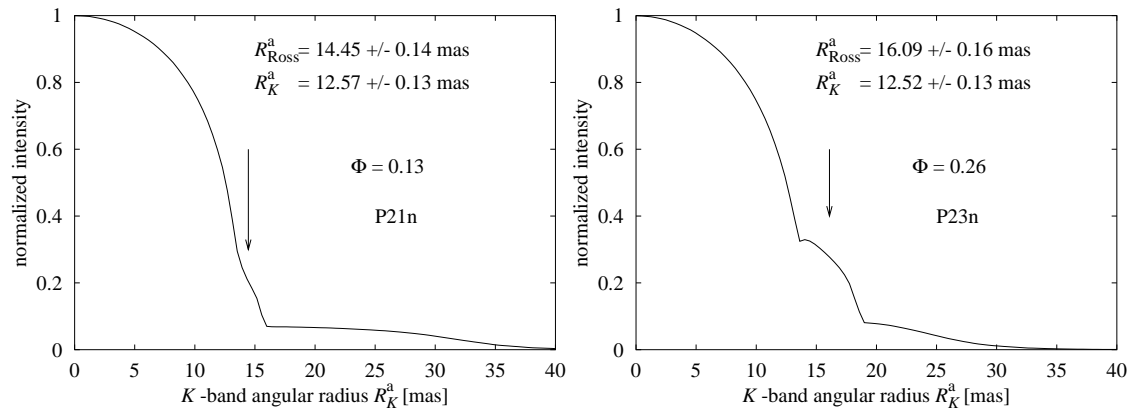


Figure 3. Theoretical CLV shapes of the ISW¹³ model P21n plotted for the K -band angular radius R_K^a corresponding to o Cet at $\Phi = 0.13$ (a) and of the ISW model P23n at $\Phi = 0.26$ (b) as a function of angular radius. The intensity is normalized to 1 at the disk center. The extended wing of the CLV for P models near maximum light is caused by water molecules in the outer region of the atmosphere. The corresponding visibility profiles are shown in Fig. 1. For each phase, the values of the K -band angular radii (R_K^a) and the Rosseland angular radii (R_{Ross}^a) are given. The arrows mark the position of the Rosseland angular radius. The protrusion seen for phase $\Phi = 0.26$ results from the strong increase of water absorption behind a shock front caused by the pulsation of the stellar atmosphere.

On the other hand, the effective temperatures derived from the observations are very close to the effective temperatures predicted by the D-model series but higher than those predicted by the P and M models. Given the definition of effective temperature $L = 4\pi\sigma R^2 T_{\text{eff}}^4$, this tells us that the P-series models are too low in luminosity, consistent with the luminosities derived in section 3.3 for o Cet. The shape of the measured visibilities for o Cet at phase $\Phi = 0.13$ are best fitted with the P model series, whereas all other model series and simple UD models show much poorer agreement with the observations. Taking all this into account, it is clear that a higher-luminosity, fundamental-mode model series is required for a more accurate modeling of o Cet.

Furthermore, we found that the observed visibility functions and diameters change considerably from phase 0.13 to phase 0.40. The Rosseland angular diameter of o Cet increases from $d_{\text{Ross}}^a = 28.9 \pm 0.3$ mas (corresponding to a Rosseland linear radius of $R_{\text{Ross}} = 332 \pm 38 R_{\odot}$) at $\Phi = 0.13$ to $d_{\text{Ross}}^a = 34.9 \pm 0.4$ mas ($R_{\text{Ross}} = 402 \pm 46 R_{\odot}$) at $\Phi = 0.4$. Thus, the diameter of o Cet increases by 18 % between these two phases, which is in good agreement with the approximately 14 % diameter increase for the oxygen-rich Mira S Lac.³⁹

REFERENCES

1. M. S. Bessell, M. Scholz, and P. R. Wood *A&A* **307**, p. 481, 1996.
2. K.-H. Hofmann, M. Scholz, and P. R. Wood *A&A* **339**, p. 846, 1998.
3. A. Tej, A. Lançon, M. Scholz, and P. R. Wood *A&A*, *in press* **412**, p. 481, 2003.
4. P. R. Wood, C. Alcock, R. A. Allsman, D. Alves, T. S. Axelrod, A. C. Becker, D. P. Bennett, K. H. Cook, A. J. Drake, K. C. Freeman, K. Griest, L. J. King, M. J. Lehner, S. L. Marshall, D. Minniti, B. A. Peterson, M. R. Pratt, P. J. Quinn, C. W. Stubbs, W. Sutherland, A. Tomaney, T. Vandehei, and D. L. Welch in *IAU Symp. 191: Asymptotic Giant Branch Stars*, eds. T. Le Bertre, A. Lèbre and C. Waelkens, p. 151, 1999.
5. M. W. Feast *MNRAS* **278**, p. 11, 1996.
6. G. T. van Belle, H. M. Dyck, J. A. Benson, and M. G. Lacasse *AJ* **112**, p. 2147, 1996.
7. F. G. Pease *Ergebn. d. Exakten Naturwiss.* **10**, p. 84, 1931.
8. C. A. Haniff, M. Scholz, and P. G. Tuthill *MNRAS* **276**, p. 640, 1995.
9. G. Weigelt, D. Mourard, L. Abe, U. Beckmann, O. Chesneau, C. Hillemanns, K. Hofmann, S. D. Ragland, D. Schertl, M. Scholz, P. Stee, N. Thureau, and F. Vakili in *Interferometry in Optical Astronomy*, eds. P. J. Léna and A. Quirrenbach, *SPIE Proc.*, 4006, p. 617, 2000.
10. T. Watanabe and K. Kodaira *PASJ* **31**, p. 61, 1979.
11. M. Scholz *A&A* **145**, p. 251, 1985.

12. M. S. Bessell, J. M. Brett, P. R. Wood, and M. Scholz *A&A* **213**, p. 209, 1989.
13. M. J. Ireland, M. Scholz, and P. R. Wood *MNRAS*, in press, 2004.
14. K.-H. Hofmann, Y. Balega, M. Scholz, and G. Weigelt *A&A* **353**, p. 1016, 2000.
15. K.-H. Hofmann, Y. Balega, M. Scholz, and G. Weigelt *A&A* **376**, p. 518, 2001.
16. G. Weigelt, U. Beckmann, J. Berger, T. Bloeker, M. K. Brewer, K. Hofmann, M. G. Lacasse, V. Malanushenko, R. Millan-Gabet, J. D. Monnier, K. Ohnaka, E. Pedretti, D. Schertl, F. P. Schloerb, M. Scholz, W. A. Traub, and B. Yudin in *Interferometry for Optical Astronomy II. ed. W. A. Traub, SPIE Proc., 4838*, p. 181, 2003.
17. M. Scholz in *Interferometry for Optical Astronomy II, ed. W. A. Traub, SPIE Proc., 4838*, p. 163, 2003.
18. G. R. Knapp, D. Pourbaix, I. Platais, and A. Jorissen *A&A* **403**, p. 993, 2003.
19. P. Kervella, P. B. Gitton, D. Segransan, E. di Folco, P. Y. Kern, M. Kiekebusch, T. P. Duc, A. Longinotti, V. Coudé du Foresto, P. Ballester, C. Sabet, W. D. Cotton, M. Schoeller, and R. Wilhelm in *Interferometry for Optical Astronomy II. ed. W. A. Traub, SPIE Proc., 4838*, p. 858, 2003.
20. V. Coudé du Foresto and S. T. Ridgway in *High-Resolution Imaging by Interferometry II, eds. Merkle F., Boeckers J. M., ESO Proc.*, p. 731, 1992.
21. J.-M. Mariotti, V. Coudé du Foresto, G. Perrin, P. Zhao, and P. Léna *A&AS* **116**, p. 381, 1996.
22. A. Labeyrie *A&A* **6**, p. 85, 1970.
23. H. C. Woodruff, M. Eberhardt, T. Driebe, K.-H. Hofmann, K. Ohnaka, A. Richichi, D. Schertl, M. Schöller, M. Scholz, G. Weigelt, M. Wittkowski, and P. R. Wood *A&A*, in press, 2004.
24. V. Coudé du Foresto, S. Ridgway, and J.-M. Mariotti *A&AS* **121**, p. 379, 1997.
25. G. Perrin *A&A* **400**, p. 1173, 2003.
26. A. Richichi and I. Percheron *A&A* **386**, p. 492, 2002.
27. ESA *VizieR Online Data Catalog* **1239**, p. 1, 1997.
28. M. Scholz and Y. Takeda *A&A* **186**, p. 200, 1987.
29. B. Baschek, M. Scholz, and R. Wehrse *A&A* **246**, p. 374, 1991.
30. J. A. Mattei private communication, 2003.
31. B. J. Smith, D. Leisawitz, M. W. Castelaz, and D. Luttermoser *AJ* **123**, p. 948, 2002.
32. B. J. Smith *AJ* **126**, p. 935, 2003.
33. L. Celis S. *AJ* **87**, p. 1791, 1982.
34. R. Wing, 2003. private communication.
35. G. W. Lockwood and R. F. Wing *ApJ* **169**, p. 63, 1971.
36. T. G. Barnes *ApJS* **25**, p. 369, 1973.
37. B. Yudin, 2003. private communication.
38. M. Schwarzschild *ApJ* **195**, p. 137, 1975.
39. R. R. Thompson, M. J. Creech-Eakman, and G. T. van Belle *ApJ* **577**, p. 447, 2002.
40. A. Tej, A. Lançon, and M. Scholz *A&A* **401**, p. 347, 2003.
41. I. Yamamura, T. de Jong, and J. Cami *A&A* **348**, p. L55, 1999.
42. M. Feast in *IAU Symp. 191: Asymptotic Giant Branch Stars, eds. T. Le Bertre, A. Lèbre and C. Waelkens*, p. 109, 1999.
43. Y. Tuchman in *IAU Symp. 191: Asymptotic Giant Branch Stars, eds. T. Le Bertre, A. Lèbre and C. Waelkens*, p. 123, 1999.